Impact of extracellular matrix and collagen network properties on the cervical intervertebral disc response to physiological loads: A parametric study

Mohamed Amine Chetoui, Dominique Ambard, Patrick Cañadas, Pascal Kouyoumdjian, Pascale Royer, Simon Le Floc'h

Impact of extracellular matrix and collagen network properties on the cervical intervertebral disc response to physiological loads: A parametric study

Mohamed Amine Chetoui[a,*], Dominique Ambard[b], Patrick Canãdas[b], Pascal Kouyoumdjian[c], Pascale Royer[b], Simon Le Floc'h[b]

[a] *Pascal Institute UMR6602, Univ. of Clermont Auvergne, Aubière, France*
[b] *LMGC UMR5508, Univ. of Montpellier, CNRS, Montpellier, France*
[c] *Orthopedic surgery and trauma service, Spine surgery, CHRU of Nîmes, Nîmes, France*

Abstract

Current intervertebral disc finite element models are hard to validate since they describe multi-physical phenomena and contain a huge number of material properties. This work aims to simplify numerical validation/identification studies by prioritizing the sensitivity of intervertebral disc behavior to mechanical properties. A 3D fiber-reinforced hyperelastic model of a C6-C7 intervertebral disc is used to carry out the parametric study. 10 parameters describing the extracellular matrix and the collagen network behaviors are included in the parametric study. The influence of varying these parameters on the disc response is estimated during physiological movements of the head, including compression, lateral bending, flexion, and axial rotation. The obtained results highlight the high sensitivity of the disc behavior to the stiffness of the annulus fibrosus extracellular matrix for all the studied loads with a relative increase in the disc apparent stiffness by 67% for compression and by 57% for axial rotation when the annulus stiffness increases from 0.4 to 2 MPa. It is also shown that varying collagen network orientation, stiffness, and stiffening in the studied configuration range have a noticeable effect on rotational motions with a relative apparent stiffness difference reaching 6.8%, 10%, and 22%, respectively, in lateral bending. However, the collagen orientation does

*Corresponding author
Email address: mohamed-amine.chetoui@centrale-marseille.fr (Mohamed Amine Chetoui)

not affect disc response to axial load.

Keywords: Intervertebral disc, FE analysis, Fibrous soft tissue, Porous media, Cervical spine kinematics.

1. Introduction

Tissue engineering, replacement and regeneration techniques are increasingly used in the treatment of intervertebral disc diseases. While synthetic material replacements are still limited by the biocompatibility hurdle, biomaterials designed for annulus fibrosus (AF) and nucleus pulposus (NP) repair and replacement have managed to mimic IVD biology and have shown promising results [1, 2]. However, without focusing on mechanical compatibility, these biomaterials-based solutions have not yet shown a long-term performance [2, 3]. Mechanical compatibility is not less critical than biocompatibility since it permits to restore biomechanical behavior of the motion segment, and thus reduces re-herniation and promotes longevity [2, 4]. Therefore, a sophisticated comprehension of the biomechanical behavior of the intervertebral disc is invaluable to enhancing the performance of biomaterial-based techniques.

The intervertebral disc (IVD) biomechanical behavior is complex and it can not be explored using only experiments or analytical methods [5]. Spine and disc biomechanics are commonly studied using finite element (FE) analysis. FE models developed for the IVD are increasingly improved. However, they become more difficult to implement and validate.

Recent models take into account complex structural phenomena taking part in this soft tissue such as the osmotic role of proteoglycans and the mechanical contribution of collagen fibers including fiber cross-links, fiber/matrix interaction, and interlamellar behavior (e.g. [6, 7, 8, 9]). These models generally managed to provide a good agreement with experimentation. However, the uniqueness of the identified mechanical properties is not guaranteed given their relatively large number and their possible interdependency [10, 11]. Furthermore, the

impact of the experimentation-related uncertainties on the identification studies remains significant and it is reflected in the large scatter of the IVD mechanical properties values. Most of the biomechanical experimental tests used in the parameter identification are performed ex-vivo. Cadaveric tissue, generally used to perform biomechanical ex-vivo experimental tests, undergoes several changes in properties related to the conservation conditions which leads to variability in the experimental data [12]. In addition, the relevance of each parameter depends on the load type and the nature of the experimental data used for the identification. For example, the micro-channels configuration of a porous medium may increase the apparent stiffness of the tissue in the case of confined consolidation compared to the unconfined one [13].

Computational validation issues could be treated by several approaches. Multi-objective optimization and the use of huge experimental databases could be suggested. However, these solutions tend to complicate the studies and raise their time-memory cost. Different approaches, based upon the exploitation of quantitative MRI for the construction and the validation of FE models were introduced [14, 11]. This technique seems efficient but is limited by the MRI resolution and needs to be clinically validated. Recent studies introduced probabilistic and deterministic deep learning approaches to reduce the cost of complex behavior tissue models including porous media, hyperelastic anisotropic tissue, and multiscale models. Despite their promising results in model reduction and simulation acceleration, these methods present some limitations related to the handle with irregular mesh and some particular boundary conditions [15, 16, 17]. Therefore, sensitivity studies remain an essential tool to improve and validate IVD FE models [18, 5]. Studying the impact of varying the parameter values permits to better understand the IVD model biomechanics and manage the validation studies. It allows sorting parameters by relevance and fixing the values of those with no significant effect, simplifying the study by focusing on the most important parameters and

therefore helping to obtain a more accurate result.

Several sensitivity analyses have been conducted on lumbar spine FE models. The impact of structural, mechanical, and morphological properties of vertebrae, IVD, and ligaments in the lumbar spine was studied under different loads [19, 20, 21, 22, 5]. The obtained results have contributed to the understanding of lumbar spine biomechanics and the studying of some FE models accuracy. However, fewer sensitivity studies have been carried out for the cervical spine and they are limited on the sensitivity of the stiffness of the spinal components, assumed to be linear elastic, on spine biomechanics [23, 24]. The current study represents a sensitivity analysis of C6-C7 IVD mechanical properties using a nonlinear poroelastic FE model with fiber reinforcement. The objective is to determine and analyze the sensitivity of the model to both the matrix mechanical properties and the collagen network configuration. For this purpose, physiological loads are used in the simulations. By prioritizing the contribution of the model properties in the IVD biomechanics for different load types, this work aims to create a benchmark for numerical studies.

2. Material and methods

2.1. Constitutive formulation

The definition of quantities of interest permits to perform the mesh sensibility test and to choose the constitutive model of the study [25]. In our case, we were interested in the maximum stress linked to the solid phase, the fluid flow linked to the fluid phase and the apparent stiffness which is a global quantity linked to the entire domain.

The choice of the constitutive model has been based on the quantities of interest and on the mechanical aspects studied in the literature. In vivo measurements have shown that the cervical IVD undergoes large strain during physiological motion [26]. It was also shown

that the collagen fibers do not contribute only to the tissue response to mechanical loads but also to its swelling behavior [27, 28]. On the other hand, The compressibility of the extracellular matrix (ECM) has been largely investigated and discussed. Although several finite element studies have adopted a nearly-incompressible model for the extracellular matrix, recent experimental studies have highlighted the auxetic compressible behavior of the annulus fibrosus [29, 30]. These results revealed the importance of studying the IVD behavior in large deformation, taking into account the annulus anisotropy, the compressibility of the extracellular matrix (ECM), and the fluid flow in the porous network.

The constitutive formulation implemented for this study is based on the biphasic swelling model [31, 32, 33]. The IVD is assimilated to a superposition of two immiscible and isothermal phases: a porous solid skeleton describing the fiber-reinforced extracellular matrix saturated by an intrinsically incompressible fluid. The total Cauchy stress $\boldsymbol{\sigma}$ is the summation of the solid effective stress tensor $\boldsymbol{\sigma}^{\boldsymbol{e}}$ and the interstitial fluid stress derived from the hydrostatic pressure p and the osmotic pressure $\Delta\pi$:

$$\boldsymbol{\sigma} = \boldsymbol{\sigma}^{\boldsymbol{e}} - (p + \Delta\pi)\mathbf{1} \tag{1}$$

The hydrostatic pressure p is determined by Darcy and mass conservation laws while respecting the intrinsic incompressibility assumption. The permeability k of the medium is taken isotropic and strain-dependent as proposed in [34]. The osmotic pressure $\Delta\pi$ of the IVD is expressed in terms of the fixed charge density of the proteoglycans C_{fc} which is also taken strain-dependent [33].

$$\Delta\pi = RT(\varphi_i\sqrt{C_{fc}^2 + 4C_e^2} - 2\varphi_e C_e) \tag{2}$$

$$C_{fc} = C_{fc0}\frac{\phi_0}{\phi_0 - 1 + J} \tag{3}$$

where ϕ_0 is the initial porosity, J is the deformation gradient determinant, C_{fc} and C_{fc0} are the current and the initial fixed charge densities respectively, C_e the external salt concentration, R the universal gas constant, T the absolute temperature, and φ_i and φ_e respectively the internal and the external osmotic coefficients. The extracellular matrix of the medium is defined by its total strain energy density W. W was composed of a compressible Neo-Hookean isotropic part W_{NH} for the non-fibrillar matrix and an anisotropic part W_{fi} describing the contribution of each family of fibers i:

$$W = W_{NH}\left(\boldsymbol{C}\right) + \sum_i W_{fi}\left(\boldsymbol{C}, \vec{e_i}\right) \tag{4}$$

$$W_{NH} = \frac{\mu}{2}\left(I_1 - 3\right) - \mu\,\ln\left(J\right) + \frac{\lambda}{2}\,\left(\ln\left(J\right)\right)^2 \tag{5}$$

where $\boldsymbol{C}$ is the right Cauchy-Green strain tensor, I_1 is its first invariant and μ and λ are the parameters of Lamé. The vector $\vec{e_i}$ represents the director vector of the fiber family i orientation. The anisotropic part was taken null in the NP and the CEP. Two families of fibers oriented by $\pm\alpha$ were considered in the AF. The fiber strain energy density of the i^{th} fibers population (i=1,2) was defined according to [35].

$$W_{fi} = \frac{a_i}{2b_i}\left(e^{b_i\left[(1-3K)I_{fi}+KI_1-1\right]^2} - 1\right) \tag{6}$$

where a_i (MPa) and b_i (unitless) are the fiber rigidity and non linearity coefficient, K is their dispersion and I_{fi} is a fiber direction invariant written as

$$I_{fi} = \boldsymbol{C} : \left(\vec{e_i} \otimes \vec{e_i}\right) \tag{7}$$

The same mechanical parameters were taken for both families of fibers: $a_i = a_{AF}$ and $b_i = b_{AF}$.

2.2. Finite element model

The unknowns of the equation system were the hydrostatic pressure p and the three-component displacement field. We have used Lagrange quadratic (P2) and linear (P1) polynomial functions for the interpolation of the displacement and the pressure, respectively.

For this study, we have developed a three-dimensional finite element model of human C6-C7 IVD. We have constructed a parametric geometry based on six experimental studies conducted on the cervical spine morphology [36, 37, 38, 39, 40, 41]. The geometry is composed of a central elliptical *nucleus pulposus* (NP) representing 26% of the total volume, a peripheral *annulus fibrosus* (AF) surrounding the NP and two cartilaginous endplates (CEP) (Fig. 1). The geometry was meshed using the software *Gmsh* [42]. A mesh refinement study was performed using 4 20-node hexahedral element meshes with different element number to check the convergence of our quantities of interest against element size. Local refinement was not considered given the absence of geometrical irregularities, high-stress gradient, or common stress concentration areas for the studied loads. The selected mesh has been composed of 5940 hexahedral elements (26106 nodes). The model was implemented in the open-source software LMGC90 [43].

2.3. Definition of the fiber orientation

The fiber orientation angle α decreases from the inner to the outer lamella of the AF [44]. To respect this property, we have defined the fiber orientation using local spatial distributions progressing continuously from the inner to the outer AF. Two parameters were defined, α_i and α_o, the fiber angle to the transverse plane, at the inner and at the outer lamella, respectively (Fig. 2.B). Given the shape of the IVD geometry, it was necessary to define a local coordinate system centered in the NP center O_{NP} and satisfying two criteria: i) For each element of the AF, fibers are defined in lamellae plane, ii) Elements of the same lamella should have

the same fiber orientation. At this stage, the shape of the annular mesh has been useful. To define this coordinate system we started with the resolution of a thermal problem in which we have imposed two different temperatures in the lateral boundary of the AF (T_{AF}) and in the NP (T_{NP}) with $T_{AF} < T_{NP}$ (Fig. 2.A). The heat flux vector in each node defines its local radial vector $\vec{e}_{r_{AF}}$. Then, we defined the axial vector $\vec{e}_{a_{AF}}$ which corresponds to the Z-axis of the global coordinate system. The tangential vector $\vec{e}_{t_{AF}}$ was determined by the cross product ($\vec{e}_{a_{AF}} \wedge \vec{e}_{r_{AF}}$). Finally, the vectors $\vec{e_1}$ and $\vec{e_2}$ were defined in each node according to this relation:

$$\vec{e_1} = cos(\alpha).\vec{e}_{t_{AF}} + sin(\alpha).\vec{e}_{a_{AF}} \tag{8}$$

$$\vec{e_2} = -cos(\alpha).\vec{e}_{t_{AF}} + sin(\alpha).\vec{e}_{a_{AF}} \tag{9}$$

2.4. Model validation

A validation process was conducted to find the reference parameter vectors to perform the sensitivity study. We have compared the behavior of our model in lateral bending, flexion, and axial rotation to experimental previous works by reproducing the applied load described in [45, 46, 47]. These experimental studies provide functions describing the C6-C7 IVD rotation when it is exposed to a 0 to 2Nm pure moment. To compare the behavior of the current model to experimental curves, we have performed 4 tests for each motion by applying 0.5, 1, 1.5, and 2Nm moments and determined the IVD orientation angle for each test. Then we have interpolated these points to find the numerical evolution function of each motion (lateral bending, flexion, and axial rotation). The interpolation function used here has been defined in the experimental studies and has the following form: $\theta = \gamma_v + \alpha_v ln(\beta_v M + 1)$. where θ and M are the rotation angle and the applied moment, respectively, and γ_v, α_v and β_v are the function parameters. In our case, we have taken $\gamma_v = 0$ for all the loads to start from 0° of

rotation when a null moment is applied. We have manually varied the model parameters to finally find a parameter vector that permits to closely reproduce the experimental behavior of the C6-C7 IVD (Fig. 3). This parameter vector will constitute the reference vector of the parametric study called for the rest of this paper "the basic model". Here, the basic model is not necessarily the best fit combination with a minimized error compared to the experimental curve. However, we are sure that, with the retained combination, the model reproduces the experimental mechanical response used in this validation step.

2.5. Boundary conditions for the parametric study

The simulations were performed under uniaxial compression and three physiological independent loads of the cervical spine: lateral bending, axial rotation, and flexion. Each load has been applied in a 3-step sequence (Fig. 4). The first step was a 2-hour preconditioning step. The bottom surface has been constrained in all directions, the remaining boundaries being constraint-free. This step permits to obtain the unloaded IVD equilibrium in which the initial osmotic pressure distribution and the unloaded IVD equilibrium swelling were established from the fixed charge density and the porosity initial fields (C_{fc0} and ϕ_0 table 2). The second step permits to simulate the head weight. A 100N creep-compressive force was applied on the top surface of the upper CEP in 8 minutes then remains constant until the equilibrium. Finally, starting from the result of the compression-creep step, we have applied a displacement-driven load to simulate the C6-C7 translations and rotations during a physiological cervical spine lateral bending, axial rotation, and flexion (Fig. 4). Data for C6-C7 kinematics in the cervical segment are obtained from in vivo measurements taken from the literature (table 1). To reproduce the experimental measurements, we have used a y-z-x sequence (corresponding to flexion/extension-axial rotation-lateral bending) to apply the C6-C7 rotations during spine movement. The center of rotation is the center of the most posterio-

inferior point of the subjacent vertebrae (C7) for lateral bending and axial rotation [48, 49]. For the flexion, the rotation center is the center of the subjacent vertebral body [50, 51].

2.6. Studied parameter range

The parametric study has been carried out by varying 10 parameters (table 2). For the NP and the AF ground substance tissues, the varied parameters were the shear modulus μ defining the ECM stiffness, the first Lamé parameter λ defining its compressibility, and the initial permeability k_0. Collagen fiber network properties have also been studied by varying their rigidity a, their nonlinearity b, and their directions (α_o and α_i). We have chosen the interval of variation of each parameter to be always in the range of values in previous numerical studies found in the literature (table 2). This choice permits testing the sensitivity of the IVD mechanical behavior to model parameters in extended ranges used in previous studies. It is important to mention that even if some cited studies do not use the same constitutive law as the actual work, they were used to define variation range for parameters equivalent to ours in their formulation. For example, we have used the value of a_{AF} in [52] even if this study does not take into consideration the fiber dispersion defined by K_{AF} in our model. We also calculated the equivalent λ_{NP} and μ_{NP} from Young modulus and Poisson's ratio provided in [53] using elastic parameter conversion formulae.

For each parameter, the reference value was managed to be at the center of the studied range. The higher and the lower values were chosen in a way to be equally distant from the reference value and to form an interval that covers as many previously used values as possible. The first simulation has been performed using the reference parameter values (basic model). Then, for each test, we have varied only one parameter. Only the two fiber orientation angles have been simultaneously varied. To make this simultaneous variation simple we have fixed the mean fiber direction at 35^o and defined the parameter $\Delta\alpha$ which represents the difference

of the mean angle from inner and outer angles: $\alpha_i = \pm(35 + \Delta\alpha)$ and $\alpha_o = \pm(35 - \Delta\alpha)$. Finally, 37 tests have been performed for each load type. A total of 1320h of computing time was needed in this study (about 220h with parallel computation) using an HPC cluster with 28 cores and 128GB of RAM.

The studied outputs for the creep-compression step were the maximal NP pressure, the maximal normal stress, the axial and radial outflow rates, the final volume change, and the final axial displacement of the upper surface. For the physiological loads, we have studied the maximal normal and shear stress, the axial and radial outflow rates, the final volume change, and the final corresponding moment applied on the upper IVD surface. We have also studied the impact of model parameters on a global output which is the apparent stiffness for the different loads. The apparent stiffness for the rotational loads was calculated about the center of rotation (Appendix).

3. Results

3.1. Compression step

During the compression step, we can differentiate two stages. The first one is the establishment of the applied force. At this stage, the axial displacement pressurizes the fluid content due to the low permeability of the tissue. The IVD swells following this pressurization until the total establishment of the force. At this instant, the pressure and the radial swelling reach their maximal values. The second stage begins when the applied force is stabilized. In this stage, the water expulsion from the IVD becomes more important, the swelling decreases and the displacement of the loaded CEP continues until the equilibrium. We measured the influence of modifying the model parameters on the NP pressure, the normal stress, and the axial and radial flow rates at the end of the first stage. We studied also two equilibrium

results which are the volume loss caused by the water expulsion and the final displacement of the loaded face which will determine the apparent stiffness of the IVD. With the basic model, the relative change in IVD height was 4.8% and the relative change in its volume was 4.3%. Figure 5 shows the effect of modifying the model parameters on the IVD response to compression. Results show that the shear modulus of the AF ground substance μ_{AF} is the most influential parameter on IVD response to compressive load. The AF compressibility λ_{AF}, affects significantly the radial flow rate. This parameter has a lower influence on the axial flow rate, the final displacement, and the volume loss but it contributes clearly to their determination. The NP and the AF permeabilities $k0_{NP}$ and $k0_{AF}$ play also an important role in the pressurization stage. The pore pressure is very sensitive to the NP permeability and the radial flow rate is highly influenced by the AF permeability. However, the permeabilities do not contribute to the equilibrium state. Apart from the fiber rigidity, no noticeable influence was found on fiber parameters. The reference apparent stiffness obtained with the basic model was about $337 N mm^{-1}$. This value depends on model parameters in a nearly linear way with high sensitivity to the AF stiffness μ_{AF} and less noteworthy dependency on fiber rigidity a_{AF} and AF compressibility λ_{AF}. No significant effect on the IVD apparent stiffness was found for the other parameters.

3.2. Lateral bending

Figure 6 illustrates the influence of modifying model parameters on the IVD response to lateral bending. The IVD normal stress, the axial flow rate, and the volume change in lateral bending were dominated by the shear modulus of the AF ground substance μ_{AF}. The radial flow rate is highly sensitive to the AF permeability and depends less on μ_{AF}. A less noticeable dependency of the IVD outputs to the AF ground substance compressibility λ_{AF} was found. Contrary to compression, we have noticed a significant dependency of the IVD behavior on

fiber parameters in lateral bending. The fiber non-linearity parameter b_{AF} has a crucial role in the determination of the shear stress, the lateral bending moment, and the volume change. Modifying the fiber rigidity a_{AF} has a noticeable effect on the same outputs. Although fiber direction parameter $\Delta\alpha$ has not the same importance in the IVD response to lateral bending, we have found that varying this parameter may affect the shear stress and the radial outflow rate. On the other hand, apart from μ_{NP}, which slightly affects the radial flow rate, the NP parameters varying in the study range has not a real influence on the IVD response to lateral bending. The apparent stiffness in lateral bending found with the basic model was about $16Nmrad^{-1}$. This value is affected by modifying b_{AF} in the first row then AF stiffness μ_{AF} and fiber rigidity a_{AF}. The dependency of the LB apparent stiffness to these parameters is nonlinear.

3.3. Flexion

Figure 7 shows the influence of modifying model parameters on the IVD response respectively to flexion. The studied outputs depend essentially on the fiber nonlinearity b_{AF} and the AF ground substance shear modulus μ_{AF}. A less significant effect of the fiber rigidity a_{AF} and orientation $\Delta\alpha$ was found. The AF permeability $k0_{AF}$ has a significant effect on the radial flow rate value. The AF ground substance compressibility λ_{AF} contributes to the determination of the normal stress and the volume change. In a similar way to lateral bending, apart from μ_{NP}, varying the NP parameters in the study range does not affect the IVD response to flexion. The apparent stiffness in lateral bending found with the basic model was about $4.4Nmrad^{-1}$. The flexion apparent stiffness depends, in a nonlinear way, on b_{AF}, μ_{AF} and a_{AF} in descending order.

3.4. Axial rotation

The results of the effect of modifying model parameters on IVD response to axial rotation are shown in figure 8. As for the other types of load, varying μ_{AF} has a high effect on the maximal stress and the flow rates in axial rotation. In addition, the permeability of the AF slightly contributes to the determination of the radial flow rate where the role of NP permeability remains negligible. The fiber parameters b_{AF} and a_{AF} role remains crucial in the determination of shear stress, the axial rotation moment, and the volume change. We note that fiber orientation contributes more significantly to the IVD response to axial rotation than its contribution to flexion and lateral bending. Similarly to the two latter motion results, the apparent stiffness value is dominated by b_{AF}, μ_{AF} and a_{AF} with a more noticeable effect of the NP shear modulus μ_{NP}. The axial rotation apparent stiffness value found with the basic parameters was $2.83 Nmrad^{-1}$.

The apparent stiffness values found with the three physiological rotations are significantly smaller than the apparent stiffness computed with $2Nm$ pure moments applied in the validation study with ($25.8 Nmrad^{-1}$ in lateral bending, $15.3 Nmrad^{-1}$ in flexion, and $24.9 Nmrad^{-1}$ in axial rotation). This comparison reveals that coupling the different rotations and translations during a physiological movement, together with the specific anisotropic hyperelastic properties of the IVD, help reduce the resulting moment that is necessary to turn the head.

4. Discussion

This study was aimed to answer a key question that precedes any study treating the IVD mechanical modeling: given the data set and objectives, to which mechanical parameters specific attention should be paid? The answer to this question permits reducing the model numerical cost by considering the appropriate assumptions or by reducing the number of parameters in the identification studies. To prioritize model parameters we have conducted a

parametric study using an anisotropic poro-hyperelastic model of the IVD and we have examined the effect of varying 10 parameters, in the literature range, on the model response to physiological day-to-day loads.

Our methodology in the definition of parameters range has been oriented to cover the most used values in literature. Therefore, it does not consist of a sensibility study where we try to find the effect of each parameter on a limited interval but of a parametric study where we have examined the parameters contribution to the IVD behavior based on the variety of these parameter values used by previous works. Although this choice imposes a very varied width of parameters range, it allows examining the utility of using very high or very low parameter values compared to the most commonly used order of magnitude. For example, the common value of b_{AF} is under 200 in the most studies [54, 52, 11, 55] but it takes a value of 300 in [56] and 1045 in [8]. The high dependency of our model on the value of b_{AF} can be explained by the use of those two extreme values.

Our study outlines the out most influence of changing the stiffness of the extracellular matrix of AF on the poro-hyperelastic behavior of the cervical disc, by taking into account creep compression, physiological relaxation movements during flexion, bending and axial rotation. It is important to cite that we have faced numerical processing issues when using a low value of μ_{AF} and we suggest using $\mu_{AF} \geq 0.8MPa$ for the same type of model. In the current study, we have found that even the AF compressibility parameters λ_{AF} had a relevant role in the determination of many output results. This influence highlights the necessity of using a compressible extracellular matrix in FE models. These results can explain why many studies using a nearly incompressible model for the IVD are validated with a low bulk modulus which does not satisfy the near incompressibility assumption for the AF (1.45 MPa in [57], 0.8 to 1.4 MPa in [11] and 0.67 MPa in [58]). Moreover, very few studies take into account transverse deformation to the traction direction, which are crucial to estimate the compressible behavior

of AF [59, 60, 61, 29, 30]. The last two experimental studies have clearly outlined, on bovine and porcine disks respectively, the auxetic behavior of AF, and both report the dependency of the apparent Poisson's ratios to the deformation amplitude, with negative Poisson's ratios in the circumferential radial plane. Therefore, on the compressible behavior of the AF, we conclude that more experimental, numerical, and theoretical studies are needed to understand the complex, non-linear auxetic behavior of the AF. On the other hand, the relevance of the λ_{NP} has not been shown in the current study. We think that the role of this parameter was hidden by its small range of study (0.1 to $0.5MPa$). However, the compressible behavior of the human NP has been clearly outlined in several experimental studies [62, 63]. This incites us to suggest using a compressible swelling material for the NP to catch its mechanical behavior except at very high strain rates or under dynamic conditions where a viscoelastic incompressible behavior could be sufficient [64, 65, 66].

As we have shown, the permeabilities of the AF and the NP do not contribute to the determination of the equilibrium state. However, the radial flow rates are sensitive to AF permeability and less sensitive to NP permeability. The latter contributes more to the determination of the pore pressure. It is known that the water exchange within the IVD is a key factor for nutrient transport and cell activity. Therefore, inaccurate estimation of the permeabilities, especially of the AF, may lead to a loss of sufficiency in the biomechanical models of treating degeneration and growth. The current strain-dependent permeability laws proposed by [34] and [67] are sufficient to investigate the IVD solid-like behavior as reported by many studies. However, given their isotropic formulation, they are not able to describe precisely the water exchange rate in the fiber-reinforced tissues like AF [11]. We anticipate that a more accurate permeability expression that depends on strain but also on collagen fiber network organization will have a higher impact on water flow rates.

Another important finding is that collagen fiber properties including rigidity, nonlinearity,

and orientation have no significant effect on the response of the IVD to compression. However, they are a determinant factor in the cases of flexion, lateral bending, and axial rotation. As mentioned previously, the high dependency of IVD behavior to the value of b_{AF} may be partially caused by the large difference between its higher and lower tested values. The fiber nonlinearity parameter is not a measurable property which makes it difficult to estimate. Therefore, on b_{AF} value, we suggest performing more oriented AF local identification studies to limit the range of variation of this parameter. Collagen fibers have high stiffness but they do not contribute to the mechanical behavior only when they are in tension. Contrary to compression, in the case of rotational motion, the strain principal directions are near to the fiber orientation angles due to the large torsion deformation, especially in axial rotation. This result comes back to the results of [34, 68] and [69] affirming that isotropic models are able to reproduce the IVD response to compression. However, as underlined by [21], it is essential to consider fiber reinforcement when studying the IVD behavior in axial rotation. Furthermore, collagen network architecture should be neatly described by namely regional orientation difference between inner/outer and posterior/anterior AF.

This study also revealed that the collagen network within the AF has a crucial role to optimize the necessary resulting moment to turn the head. In combination with the relative movements of the adjacent vertebrae during axial rotation, lateral bending, and flexion, the mechanical properties of the collagen fiber network appear to be particularly well adapted to reduce the resulting moment by an order of magnitude compared to pure rotations. This key feature has to be taken into account while designing IVD implants.

To take back the main aim of this study, we suggest simplifying IVD model validation studies by reducing the number of identified parameters depending on the experimental optimization objective and load type. (1) For tests in statics, very slow loading tests, and when the experimental object is not time-dependent such as force-displacement curve, there is no

need to identify the permeability value. (2) For fiber-reinforced models, fiber orientation and nonlinearity should not be included in the identified parameter except when studying IVD response to rotational motion. Fiber rigidity is a determinant parameter for all types of load. (3) None of the mechanical parameters of the extracellular matrix of the AF could be neglected in the identification process. High attention should be paid to the determination of the stiffness of the AF ground substance.

Some sources of uncertainty could be identified from the current results. On a numerical level, the results of this study are provided without focusing on the uncertainty quantification of each parameter in the validation step. However, we can identify some parameters with infinite uncertainty such as the two permeabilities for stationary analysis or the fiber orientation for the uniaxial load. In the identification studies, the accuracy of the model needs to be investigated by uncertainty quantification. This will be useful to localize the optimal experimental fields to measure, design accurate experiments and therefore minimize model error [72, 73, 74]. On a physiological level, only the IVD prestress related to the osmotic pressure was included. However, a second part, related to the gradient of tissue growth could be taken into account. The IVD prestress was studied for bovine and porcine tissues [75, 76, 77, 29] but no data concerning human disc prestress are yet provided in the literature to our knowledge. In addition, the loading conditions, taken from previous experimental studies, may affect the current results given the non linear anisotropic behavior of the model.

Our study, which focused on varying each parameter independently of the others, revealed the complex mechanical behavior in in-vivo solicitations. In future work, the variation of multiple parameters at the same time will be performed. We anticipate this scheme may reveal coupled effects and allow more efficient simplifications of the validation studies.

Nomenclature

$\boldsymbol{\sigma}$	Total Cauchy stress tensor
$\boldsymbol{\sigma}^e$	Solid phase effective stress tensor
$\boldsymbol{C}$	Right Cauchy-Green strain
$\vec{e}_i$	Director vector of the i^{th} fiber family
p	Fluid phase hydrostatic pressure (Pa)
$\Delta\pi$	Osmotic pressure (Pa)
k_0	initial permeability $(m^4 N^{-1} s^{-1})$
C_{fc}	Fixed charge density $(mol\ m^{-3})$
C_{fc0}	Initial fixed charge density $(mol\ m^{-3})$
ϕ_0	Initial porosity (unitless)
J	Deformation gradient determinant
μ	Shear modulus (Pa)
λ	First Lamé parameter (Pa)
a_i	Fiber rigidity (Pa)
b_i	Fiber non linearity coefficient (unitless)
K	Fiber dispersion coefficient (unitless
I_{fi}	Direction invariant of the i^{th} family fiber
α_i	Inner fiber orientation $(^\circ)$
α_o	Outer fiber orientation $(^\circ)$
$\Delta\alpha$	$(\alpha_i - \alpha_o)/2\,(^\circ)$

Constants

R universal gaz constant $=8.314 J\ mol^{-1}.K^{-1}$

T Absolute temperature $=310K$

C_e External salt concentration $=150 mol\ m^{-3}$

φ_i Internal osmotic coefficient $=0.9$

φ_e External osmotic coefficient$=0.9$

Appendix: Apparent stiffness

The head-weight force in compression and the coupled displacements in the other physiological loads were applied on the upper surface of the disc which is assumed to be rigid. The apparent stiffness is calculated using the applied load or displacement and the resulting displacement or external force, respectively. For compression, the apparent stiffness $A_{pp}S(Nm^{-1})$ is defined as:

$$A_{pp}S = \left|\frac{F_{app}}{w_{res}}\right|$$

where $F_{app}(N)$ is the applied force and $w_{res}(m)$ is the displacement of the upper surface in the z direction (the same direction as the applied force).

For the other physiological loads, the apparent stiffness $A_{pp}S(Nm\ rad^{-1})$ is defined as:

$$A_{pp}S = \left|\frac{\vec{M}_{res}.\vec{e}_p}{\varphi_{app}}\right|$$

where $\vec{M}_{res}(Nm)$ is the global moment of the upper surface points about the center of rotation, $\varphi_{app}(rad)$ is the global cervical segment rotation as described in the table 1 and $\vec{e}_p$ the principal direction of the rotation: $\vec{x}$ for flexion, $\vec{y}$ for lateral bending and $\vec{z}$ for axial rotation. $M_{res}(Nm)$ is obtained according to this equation:

$$\vec{M}_{res} = \iint_{up} \vec{M}_{n,res} dS = \iint_{up} \left(O\vec{M}_n \wedge \vec{F}_{n,res}\right) dS$$

where $\vec{M}_{n,res}(Nm)$ is the resulting nodal moment, $\vec{F}_{n,res}(N)$ the resulting nodal force, and $O\vec{M}_n(m)$ the final nodal position with regard to the center of rotation.

Conflict of interests

The authors declare that they have no conflict of interests to disclose.

Ethical approval

Not required

Source of funding

This work has been supported by MESO@LR Platform of the University of Montpellier, by Labex NUMEV (ANR-10-LABX-20 projects 2017-1-27) and by CNRS (AAP "Osez l'interdesciplinarité 2018", MoTiV Project)

References

[1] Zhuang Y, Huang B, Li CQ, Liu LT, Pan Y, Zheng WJ, Luo G, Zhou Y. Construction of tissue-engineered composite intervertebral disc and preliminary morphological and biochemical evaluation. Biochem Biophys Res Commun 2011;407(2):327–32.

[2] D'Este M, Eglin D, Alini M. Lessons to be learned and future directions for intervertebral disc biomaterials. Acta Biomater 2018;78:13–22.

[3] Buckley CT, Hoyland JA, Fujii K, Pandit A, Iatridis JC, Grad S. Critical aspects and challenges for intervertebral disc repair and regeneration-harnessing advances in tissue engineering. JOR Spine 2018;1(3):e1029.

[4] Sharabi M, Wertheimer S, Wade KR, Galbusera F, Benayahu D, Wilke HJ, Haj-Ali R. Towards intervertebral disc engineering: Bio-mimetics of form and function of the annulus fibrosus lamellae. J Mech Behav Biomed Mater 2019;94:298–307.

[5] Guo LX, Fun W. Impact of material properties of intervertebral disc on dynamic response of the human lumbar spine to vertical vibration: A finite element sensitivity study. Med Biol Eng Comput 2019;57(1):221–9.

[6] Hollingsworth NT, Wagner DR. Modeling shear behavior of the annulus fibrosus. J Mech Behav Biomed Mater 2011;4(7):1103–14.

[7] Reutlinger C, Bürki A, Brandejsky V, Ebert L, Büchler P. Specimen specific parameter identification of ovine lumbar intervertebral discs: On the influence of fibre-matrix and fibre-fibre shear interactions. J Mech Behav Biomed Mater 2014;30:279–89.

[8] Mengoni M, J. Luxmoore BJ, N. Wijayathunga VN, Jones AC, Broom ND, Wilcox RK. Derivation of inter-lamellar behaviour of the intervertebral disc annulus, J Mech Behav Biomed Mater 2015;48:164–72.

[9] Masni-Azian, Tanaka M. Biomechanical investigation on the influence of the regional material degeneration of an intervertebral disc in a lower lumbar spinal unit: A finite element study. Comput Biol Med 2018;98:26–38.

[10] Oreskes N. Evaluation (not validation) of quantitative models. Environ Health Perspect 1998;106:1453–1460.

[11] Chetoui MA, Boiron O, Ghiss M, Dogui A, Deplano V. Assessment of intervertebral disc degeneration-related properties using finite element models based on ρ_h-weighted MRI data. Biomech Model Mechanobiol 2019;18(1):17–28.

[12] Olson SA, Marsh JL, Anderson DD, Latta Pe LL. Designing a biomechanics investigation: choosing the right model. J Orthop Trauma 2012;26(12):672-7.

[13] Urcun S, Rohan PY, Sciumè G, Bordas SPA. Cortex tissue relaxation and slow to medium load rates dependency can be captured by a two-phase flow poroelastic model. J Mech Behav Biomed Mater 2022;126:104952.

[14] Stadelmann MA, Maquer G, Voumard B, Grant A, Hackney DB, Vermathen P, Alkalay RN, Zysset PK. Integrating MRI-based geometry, composition and fiber architecture in a finite element model of the human intervertebral disc. J Mech Behav Biomed Mater 2018;85:37–42.

[15] Thakolkaran P, Joshi A, Zheng Y, Flaschel M, De Lorenzis L, Kumar S. NN-EUCLID: Deep-learning hyperelasticity without stress data. In: Pre-print under review (2022). arXiv: 2205.06664.

[16] Krokos V, Bui Xuan V, Bordas SPA, Young P, Kerfriden P. A Bayesian multiscale CNN framework to predict local stress fields in structures with microscale features. Comput Mech 2022;69:733–66.

[17] Deshpande S, Lengiewicz J, Bordas SP. Probabilistic deep learning for real-time large deformation simulations. Comput Methods Appl Mech Eng 2022;398:115307.

[18] Anderson AE, Ellis BJ, Weiss JA. Verification, validation and sensitivity studies in computational biomechanics. Comput Methods Biomech Biomed Eng 2007;10(3):171–84.

[19] Malandrino A, Planell JA, Lacroix D, Statistical factorial analysis on the poroelastic material properties sensitivity of the lumbar intervertebral disc under compression, flexion and axial rotation. J Biomech 2006;42(16):2780–88.

[20] Jebaseelan DD, Jebaraj C, Yoganandan N, Rajasekaran S, Kanna RM. Sensitivity studies of pediatric material properties on juvenile lumbar spine responses using finite element analysis. Med Biol Eng Comput 2012;50(5):515–22.

[21] Yang B, O'Connell GD. Effect of collagen fiber orientation on intervertebral disc torsion mechanics. Biomech Model Mechanobiol 2017;16(6):2005–15.

[22] Zander T, Dreischarf M, Timm AK, Baumann WW, Schmidt H. Impact of material and morphological parameters on the mechanical response of the lumbar spine – a finite element sensitivity study. J Biomech 2017;53:185–90.

[23] Kumaresan S, Yoganandan N, Pintar FA. Finite element analysis of the cervical spine: A material property sensitivity study. Clin Biomech 1999;14(1):41–53.

[24] Ng HW, Teo EC, Lee VS. Statistical factorial analysis on the material property sensitivity of the mechanical responses of the C4-C6 under compression, anterior and posterior shear. J Biomech 2004;37(5):771–7.

[25] Duprez M, Bordas SPA, Bucki M, Bui HP, Chouly F, Lleras V et al. Quantifying discretization errors for soft tissue simulation in computer assisted surgery: A preliminary study. Applied Mathematical Modelling 2020;77:709–23.

[26] Anderst W, Donaldson W, Lee J, Kang J. Cervical Spine Disc Deformation During In Vivo Three-Dimensional Head Movements. Ann Biomed Eng 2016;44(5):1598-612

[27] Sharabi M, Wade K, Haj-Ali R. The Mechanical Role of Collagen Fibers in the Intervertebral Disc. In: Galbusera F, Wilke HJ, editors. Biomechanics of the Spine, Academic Press;2018, p. 105–23

[28] Yang B, O'Connell GD. Swelling of fiber-reinforced soft tissues is affected by fiber ori-

entation, fiber stiffness, and lamella structure. Journal of the Mechanical Behavior of Biomedical Materials 2018;82:320–8.

[29] Dusfour G, Maumus M, Cañadas P, Ambard D, Jorgensen D, Noël D, Le Floc'h S. Mesenchymal stem cells-derived cartilage micropellets: A relevant in vitro model for biomechanical and mechanobiological studies of cartilage growth. Mater Sci Eng: C 2020;112:110808.

[30] Derrouiche A, Karoui A, Zaïri F, Ismail J, Qu Z, Chaabane M, Zaïri F. The two poisson's ratios in annulus fibrosus: Relation with the osmo-inelastic features. Mech Soft Mater 2020;2:1.

[31] Mow VC, Kuei SC, Lai WM, Armstrong CG. Biphasic creep and stress relaxation of articular cartilage in compression: Theory and experiment. J Biomech Eng 1980;102(1):73–84.

[32] Lanir Y. Biorheology and fluid flux in swelling tissues. I. Bicomponent theory for small deformations, including concentration effects. Biorheology 1987;24(2):173–87.

[33] Wilson W, Donkelaar CV, Huyghe JM, Armstrong CG. A comparison between mechano-electrochemical and biphasic swelling theories for soft hydrated tissues. J Biomech Eng 2005;127(1):158–65.

[34] Argoubi M, Shirazi-Adl A. Poroelastic creep response analysis of a lumbar motion segment in compression. J Biomech 1996;29(10):1331–9.

[35] Gasser T, Ogden R, Holzapfel G. Hyperelastic modelling of arterial layers with distributed collagen fibre orientation. J Roy Soc Interface 2006;3(6):15–35.

[36] Gilad I, Nissan M. A study of vertebra and disc geometric relations of the human cervical and lumbar spine. Spine 1986;11(2):154–7.

[37] Frobin W, Leivseth G, Biggemann M, Brinckmann P. Vertebral height, disc height, posteroanterior displacement and dens–atlas gap in the cervical spine: Precision measurement protocol and normal data. Clin Biomech 2002;17(6):423–31.

[38] Wiegand R, Kettner NW, Brahee D, Marquina N. Cervical spine geometry correlated to cervical degenerative disease in a symptomatic group. J Manip and Physiol Ther 2003;26(6):341–6.

[39] Pitzen T, Schmitz B, Georg T, Barbier D, Beuter T, Steudel WI, Reith W. Variation of endplate thickness in the cervical spine, Eur Spine J 2004;13(3):235–40.

[40] Lou J, Liu H, Rong X, Li H, Wang B, Gong Q. Geometry of inferior endplates of the cervical spine. Clinical Neurology And Neurosurgery 2016;142:132–6.

[41] Yu Y, Mao H, Li JS, Tsai TY, Cheng L, Wood KB, et al. Ranges of cervical intervertebral disc deformation during an in vivo dynamic flexion-extension of the neck. J Biomech Eng 2017;139(6):0645011–7.

[42] Geuzaine C, Remacle J. Gmsh: A 3-D finite element mesh generator with built-in pre- and post-processing facilities. Int J Num Meth Eng 2009;79(11):1309–31.

[43] Dubois F, Jean M, Renouf M, Mozul R, Martin A, Bagnéris M. Lmgc90. CSMA 2011, Giens, France. hal-00596875. doi:www.git-xen.lmgc.univ-montp2.fr/lmgc90/lmgc90_user/wikis/home.

[44] Holzapfel GA, Schulze-Bauer CA, Feigl G, Regitnig P. Single lamellar mechanics of the human lumbar anulus fibrosus. Biomech Model Mechanobiol 2005;3(10):125–40.

[45] Yoganandan N, Pintar FA, Stemper BD, Wolfla CE, Shender BS, Paskoff G. Level-dependent coronal and axial moment-rotation corridors of degeneration-free cervical spines in lateral flexion. J bone and joint surgey 2007;89(5):1066-74.

[46] Wheeldon JA, Pintar FA, Knowles S, Yoganandan N. Experimental flexion/extension data corridors for validation of finite element models of the young, normal cervical spine. J Biomech 2006;39(6):375–80.

[47] Yoganandan N, Stemper BD, Pintar FA, Baisden JL, Shender BS, Paskoff G. Normative segment-specific axial and coronal angulation corridors of subaxial cervical column in axial rotation 2008; Spine 33(5):490–6.

[48] Ishii T, Mukai Y, Hosono N, Sakaura H, Fujii R, Nakajima Y, Tamura Y, Iwasaki M, Yoshikawa H, Sugamoto K. Kinematics of the cervical spine in lateral bending: In vivo three-dimensional analysis. Spine 2006;31(2):155–60.

[49] Lin CC, Lu TW, Wang TM, Hsu CY, Hsu SJ, Shih TF. In vivo three-dimensional intervertebral kinematics of the subaxial cervical spine during seated axial rotation and lateral bending via a fluoroscopy-to-CT registration approach. J Biomech 2014;47(13):3310–7.

[50] Crawford N, Yamaguchi G, Dickman C. Methods for determining spinal flexion/extension, lateral bending, and axial rotation from marker coordinate data: Analysis and refinement. Human Movement Sci 1996;15(1):55–78.

[51] Anderst WJ, Donaldson WF 3rd, Lee JY, Kang JD. Three-dimensional intervertebral kinematics in the healthy young adult cervical spine during dynamic functional loading. J Biomech 2015;48(7):1286–93.

[52] Jacobs NT, Cortes DH, Peloquin JM, Vresilovic EJ, Elliott DM. Validation and application of an intervertebral disc finite element model utilizing independently constructed tissue-level constitutive formulations that are nonlinear, anisotropic, and time-dependent. J Biomech 2014;47(11):2540–6.

[53] Ferguson SJ, Ito K, Nolte LP. Fluid flow and convective transport of solutes within the intervertebral disc. J Biomech 2004;37(2):213–21.

[54] Ayturk UM, Gadomski B, Schuldt D, Patel V, Puttlitz CM. Modeling degenerative disk disease in the lumbar spine: a combined experimental, constitutive, and computational approach. J Biomech eng 2012;134(10):101003.

[55] Honegger JD, Actis J, Gates DH, Silverman AK, Munson AH, Petrella AJ. Development of a multiscale model of the human lumbar spine for investigation of tissue loads in people with and without a transtibial amputation during sit-to-stand. Biomech Model Mechanobiol 2021;20(1):339–58.

[56] Castro AP, Wilson W, Huyghe JM, Ito K, Alves JL. Intervertebral disc creep behavior assessment through an open source finite element solver. J Biomech 2014;47(1):297–301.

[57] Schmidt H, Reitmaier S, Is the ovine intervertebral disc a small human one? A finite element model study, J Mech Behav Biomed Mater 2013;17:229–41.

[58] Galbusera F, Schmidt H, Noailly J, Malandrino A, Lacroix D, Wilke HJ, Shirazi-Adl A. Comparison of four methods to simulate swelling in poroelastic finite element models of intervertebral discs. J Mech Behav Biomed Mater 2011;4(7):1234–41.

[59] Acaroglu ER, Iatridis JC, Setton LA, Foster RJ, Mow VC, Weidenbaum M. Degeneration and aging affect the tensile behavior of human lumbar annulus fibrosus. Spine 1995;20(24):2690–701.

[60] Elliott DM, Setton LA. Anisotropic and inhomogeneous tensile behavior of the human annulus fibrosus: Experimental measurement and material model predictions. J Biomech Eng 2001;123(3):256–63.

561 [61] Baldit A, Ambard D, Cherblanc F, Royer P. Experimental analysis of the trans-
562 verse mechanical behaviour of annulus fibrosus tissue. Biomech Model Mechanobiol
563 2014;13(3):643–52.

564 [62] Cloyd JM, Malhotra NR, Weng L, Chen W, Mauck RL, Elliott DM. Material properties
565 in unconfined compression of human nucleus pulposus, injectable hyaluronic acid-based
566 hydrogels and tissue engineering scaffolds. Eur Spine J 2007;16(11):1892–8.

567 [63] Johannessen W, Elliott DM. Effects of degeneration on the biphasic material properties
568 of human nucleus pulposus in confined compression. Spine 2005;30(24):E724–9.

569 [64] Iatridis JC, Weidenbaum M, Setton LA, Mow VC. Is the nucleus pulposus a solid or a
570 fluid? mechanical behaviors of the nucleus pulposus of the human intervertebral disc.
571 Spine 1996;21(10):1174–84.

572 [65] Iatridis JC, Setton LA, Weidenbaum M, Mow VC, The viscoelastic behavior of the non-
573 degenerate human lumbar nucleus pulposus in shear. J Biomech 1997;30(10):1005–13.

574 [66] Leahy JC, Hukins DWL. Viscoelastic properties of the nucleus pulposus of the interver-
575 tebral disk in compression. J Mater Sci: Mater Med 2001;12(8):689–92.

576 [67] Gu WY, Yao H, Huang CY, Cheung HS. New insight into deformation-dependent hy-
577 draulic permeability of gels and cartilage, and dynamic behavior of agarose gels in con-
578 fined compression. J Biomech 2003;36(4):593–8.

579 [68] Cortes DH, Jacobs NT, DeLucca JF, Elliott DM. Elastic, permeability and swelling
580 properties of human intervertebral disc tissues: A benchmark for tissue engineering. J
581 Biomech 2014;47(9):2088–94.

582 [69] Chetoui MA, Boiron O, Dogui A, Deplano V. Prediction of intervertebral disc mechanical

583 response to axial load using isotropic and fiber reinforced FE models. Comput Methods
584 Biomech Biomed Eng 2017;20:S39–S40.

585 [70] Ruiz C, Noailly J, Lacroix D. Material property discontinuities in intervertebral disc
586 porohyperelastic finite element models generate numerical instabilities due to volumetric
587 strain variations. J Mech Behav Biomed Mater 2013;26:1–10.

588 [71] Lu Y, Maquer G, Museyko O, Püschel K, Engelke K, Zysset P, Morlock M, Huber G.
589 Finite element analyses of human vertebral bodies embedded in polymethylmethalcrylate
590 or loaded via the hyperelastic intervertebral disc models provide equivalent predictions
591 of experimental strength. J Biomech 2014;47(10):2512–6.

592 [72] Sutula D, Elouneg A, Sensale M, Chouly F, Chambert J, Lejeune A et al. An open source
593 pipeline for design of experiments for hyperelastic models of the skin with applications
594 to keloids. J Mech Behav Biomed Mater 2020; 112:103999

595 [73] Elouneg A, Sutula D, Chambert J, Lejeune A, Bordas SPA, Jacquet E. An open-source
596 FEniCS-based framework for hyperelastic parameter estimation from noisy full-field data:
597 Application to heterogeneous soft tissues. Computers & Structures 2021;255:106620

598 [74] Mazier A, Bilger A, Forte AE, Peterlik I, Hale JS, Bordas SPA. Inverse deformation anal-
599 ysis: an experimental and numerical assessment using the FEniCS Project. Engineering
600 with Computers 2022. https://doi.org/10.1007/s00366-021-01597-z.

601 [75] Duclos SE, Michalek AJ. Residual strains in the intervertebral disc annulus fibrosus
602 suggest complex tissue remodeling in response to in-vivo loading. J Mech Behav Biomed
603 Mater 2017;68:232—238

604 [76] Mengoni M, Kayode O, Sikora SNF, Zapata-Cornelio FY, Gregory DE, Wilcox RK.

Annulus fibrosus functional extrafibrillar and fibrous mechanical behaviour: experimental and computational characterisation. R Soc Open Sci 2017;4(8):170807

[77] Michalek AJ, Gardner-Morse MG, Iatridis JC. Large residual strains are present in the intervertebral disc annulus fibrosus in the unloaded state. J Biomech 2012;45(7):1227-31

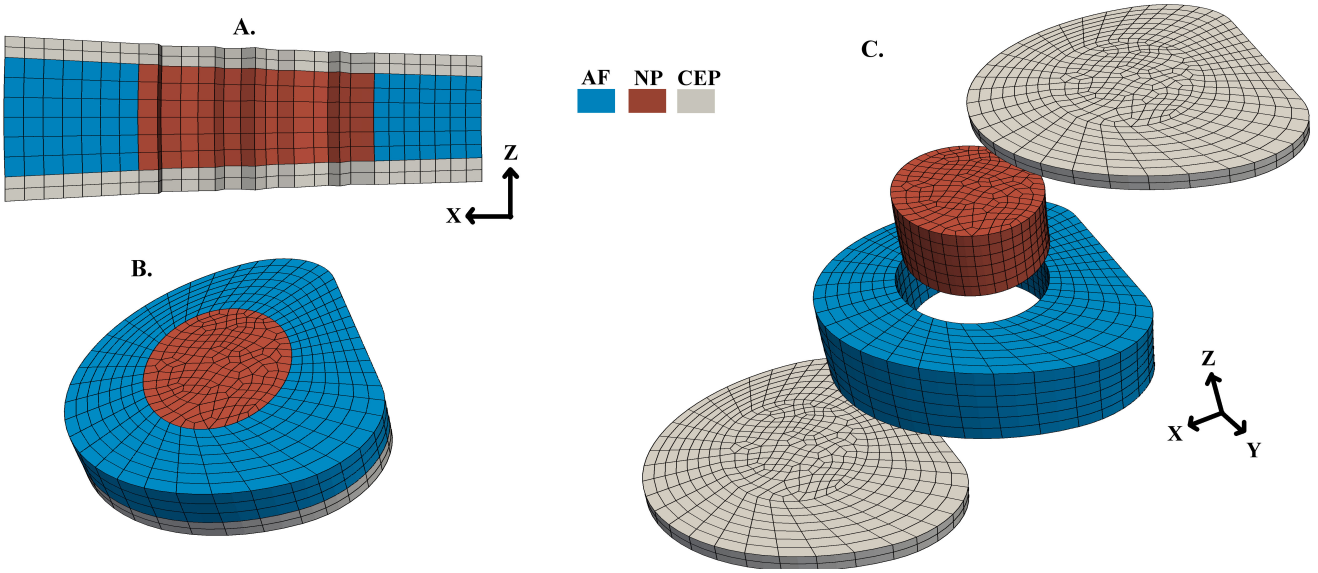

Figure 1: Geometry of C6-C7 IVD. A. Sagittal section. B. Transverse section. C. Exploded view.

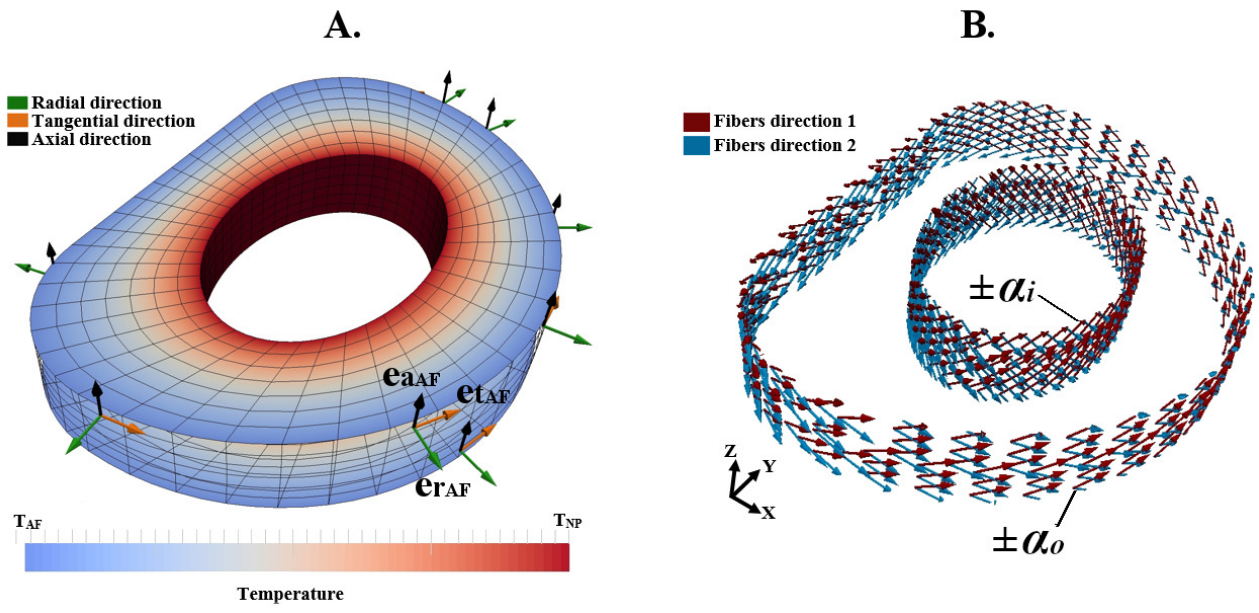

Figure 2: Definition of fiber orientation. A. Thermal solution and definition of the new coordinate system. B. Fibers directions in the inner and the outer lamellae of the AF

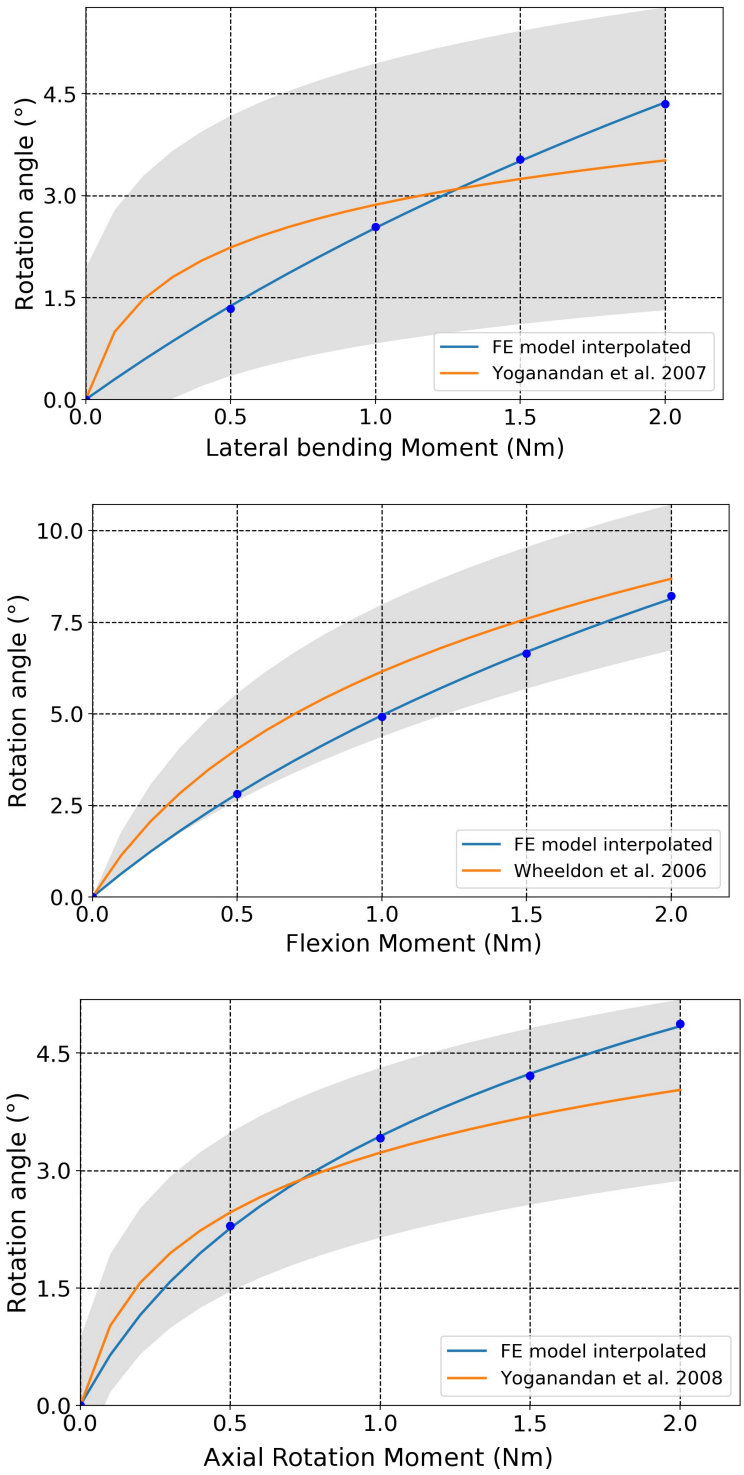

Figure 3: Experimental vs numerical response of the C6-C7 IVD to a pure moment load

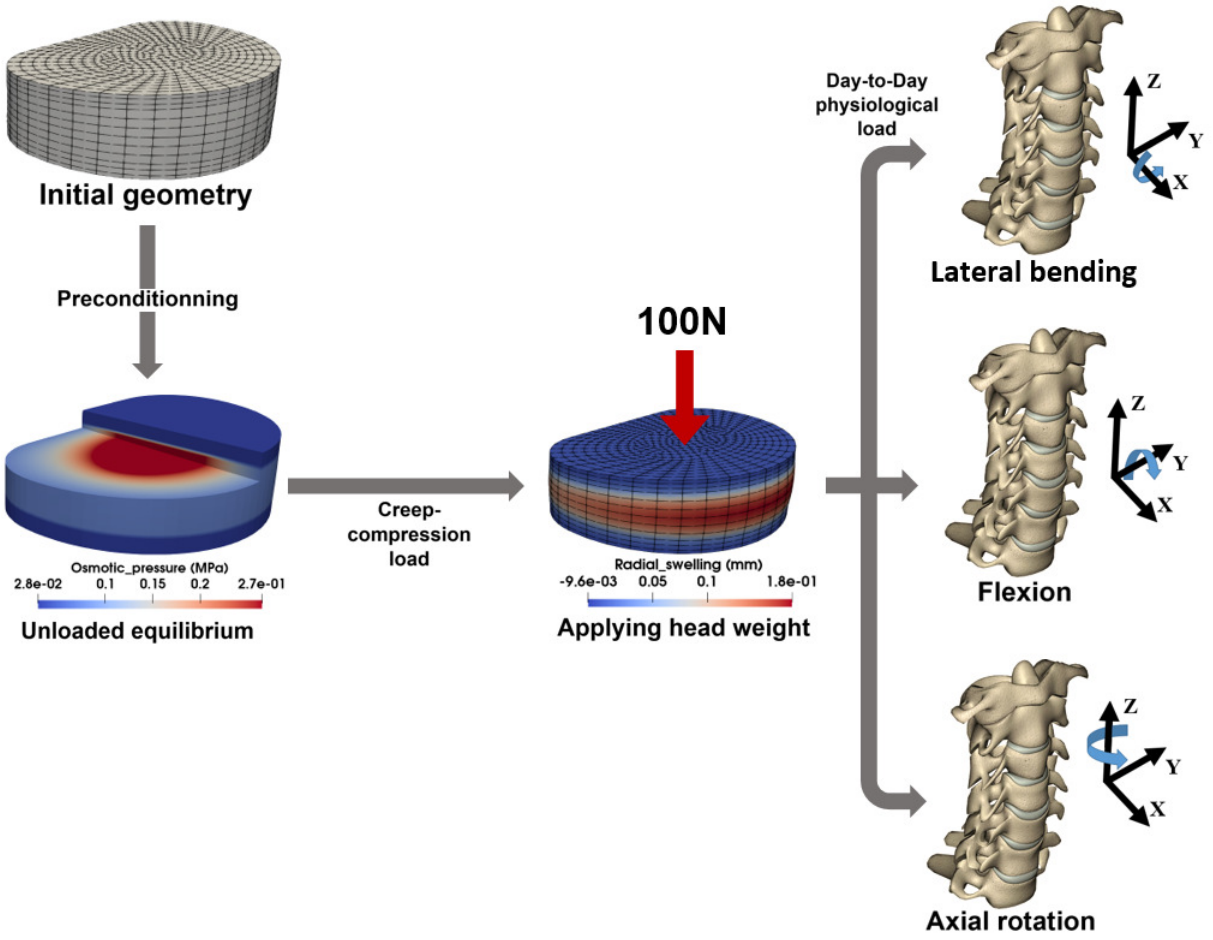

Figure 4: Representation of the IVD model simulation steps

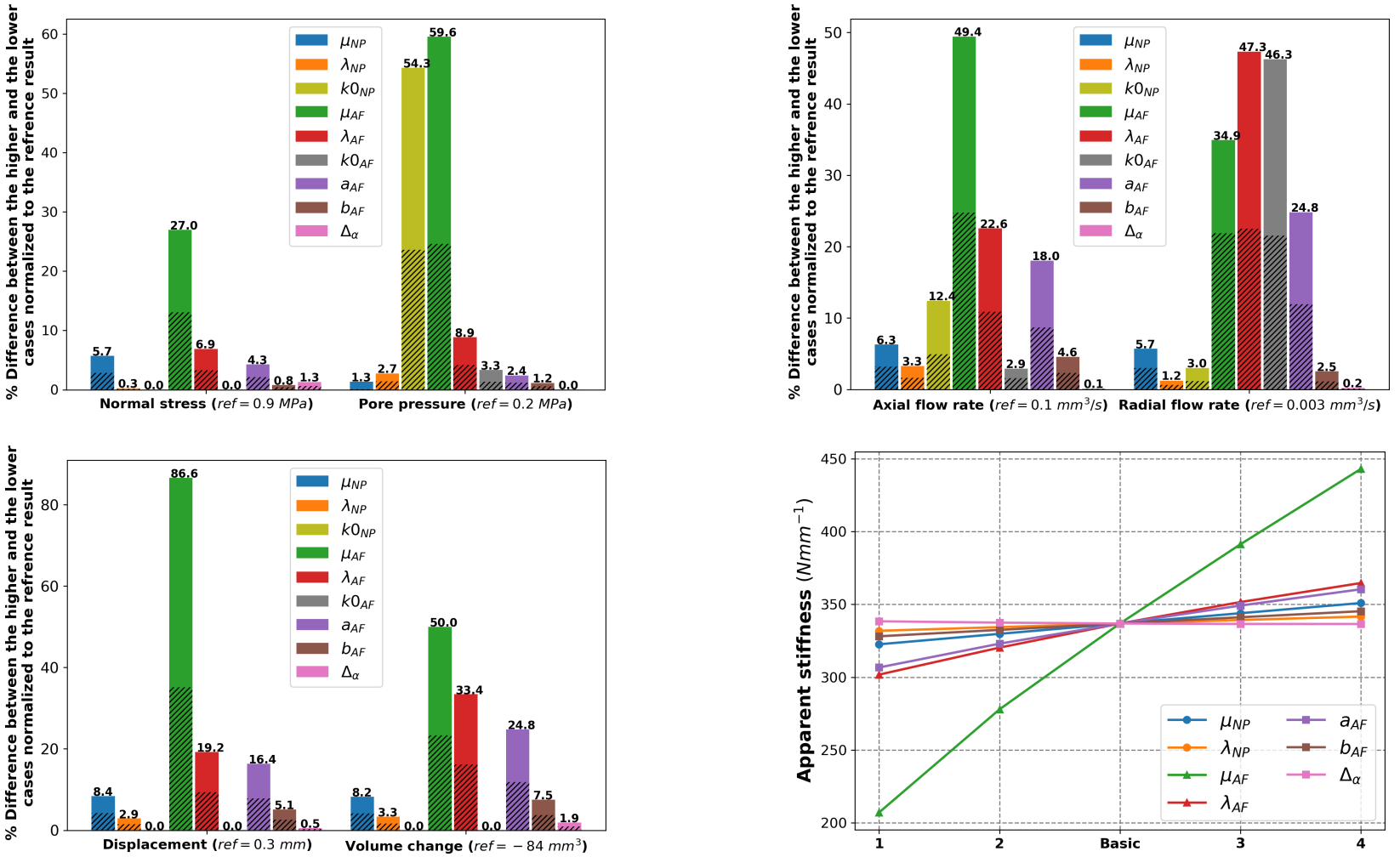

Figure 5: Impact of model parameters on IVD response to compression. The bar charts: difference between the 1 and the 4 cases (the 2 and 3 for the hatched area) normalized to the reference result (ref) obtained with the basic model parameters. The line graph corresponds to the evolution of the apparent stiffness in compression with the different scenarios of 7 parameters.

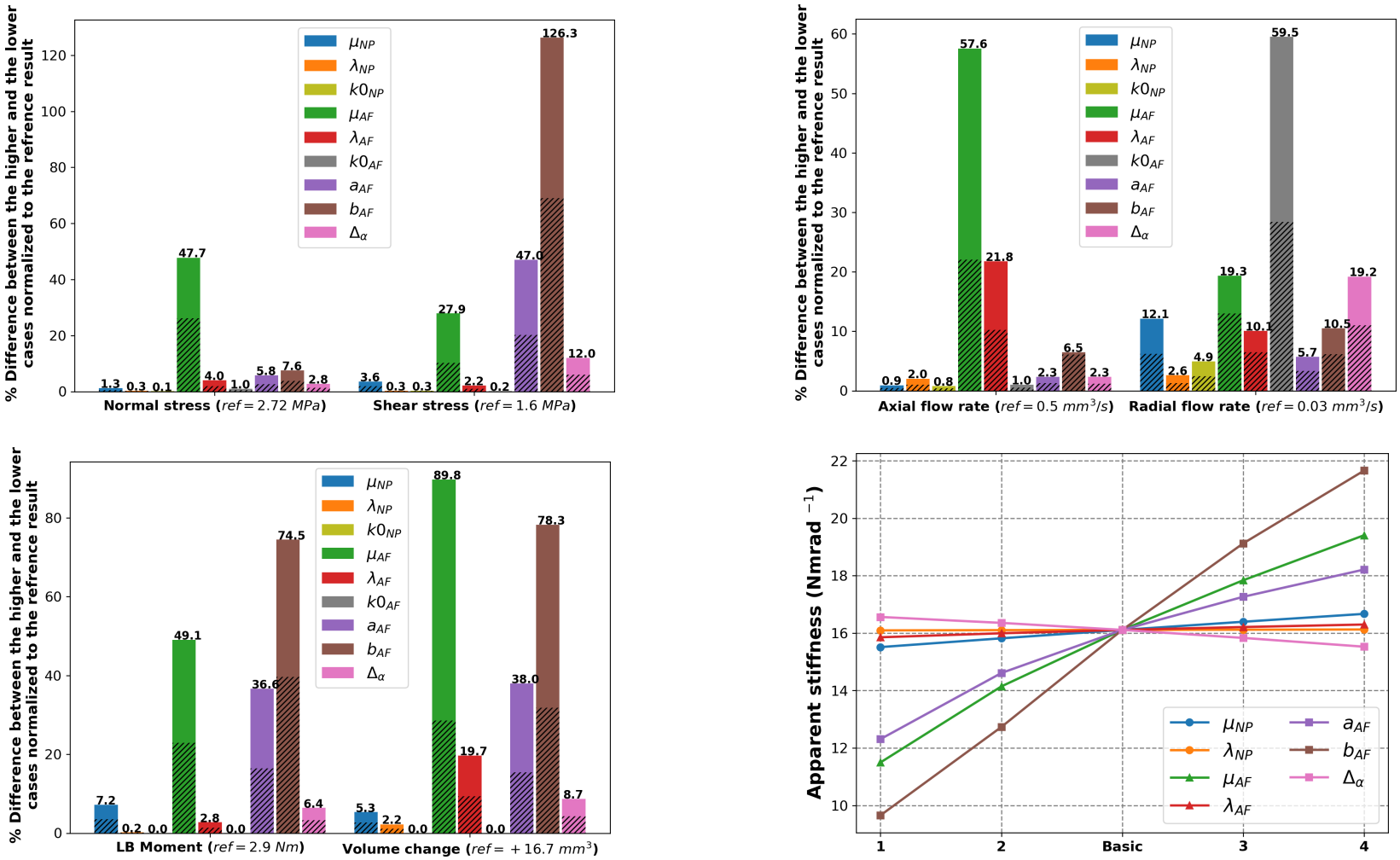

Figure 6: Impact of model parameters on IVD response to lateral bending. The bar charts: difference between the 1 and the 4 cases (the 2 and 3 for the hatched area) normalized to the reference result (ref) obtained with the basic model. The line graph corresponds to the evolution of the apparent stiffness in lateral bending with the different scenarios of 7 parameters.

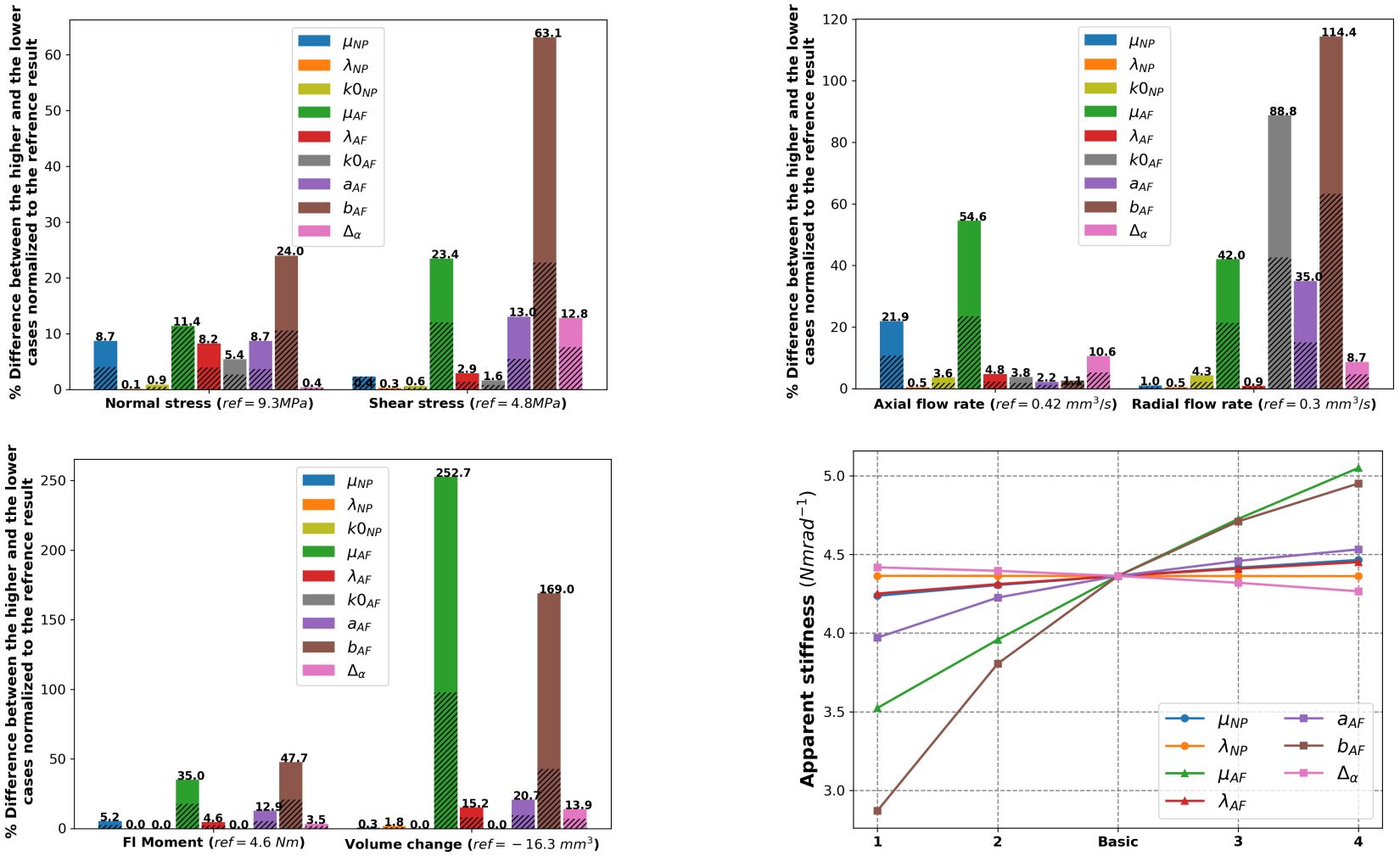

Figure 7: Impact of model parameters on IVD response to flexion. The bar charts: difference between the 1 and the 4 cases (the 2 and 3 for the hatched area) normalized to the reference result (ref) obtained with the basic model. The line graph corresponds to the evolution of the apparent stiffness in flexion with the different scenarios of 7 parameters.

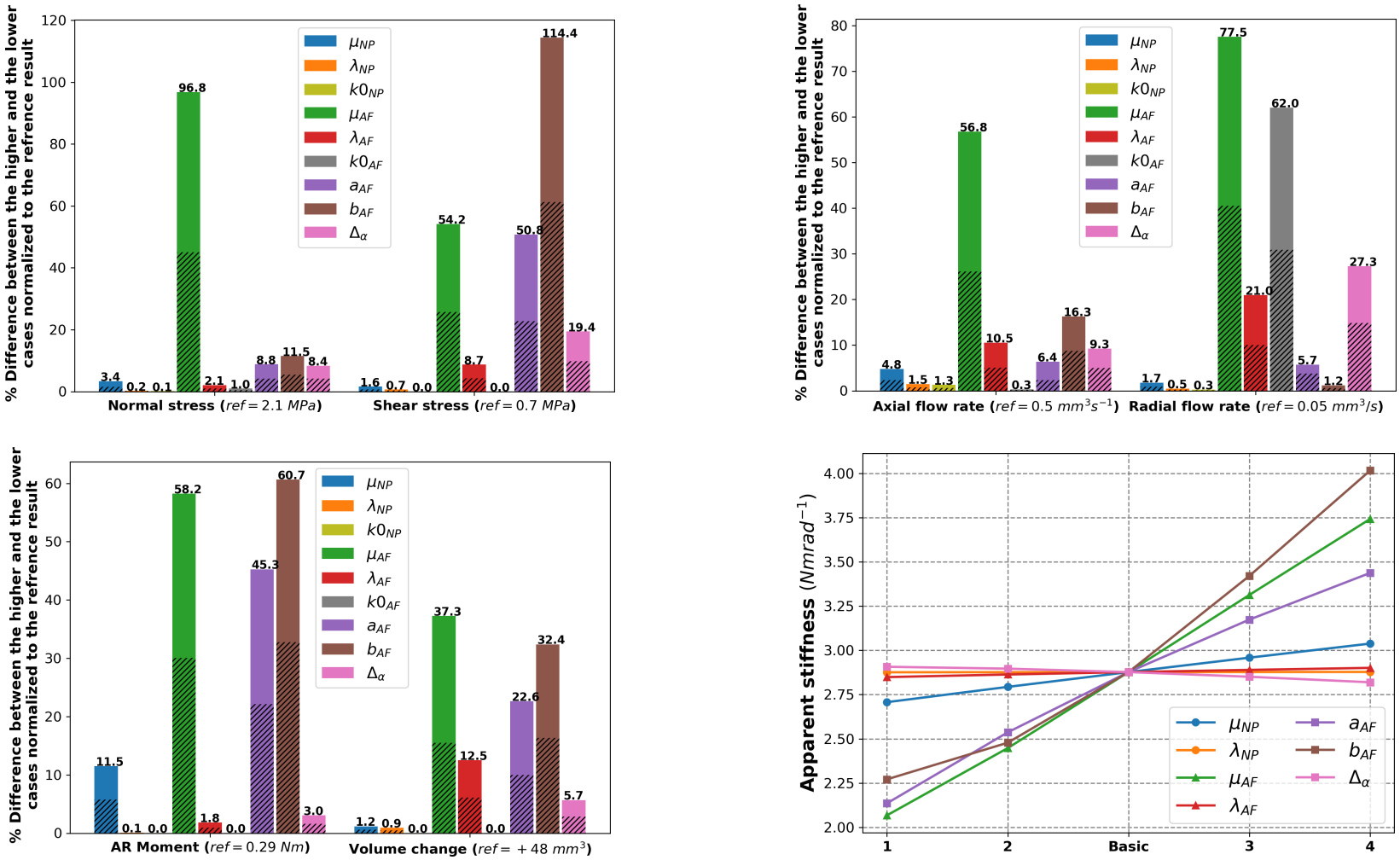

Figure 8: Impact of model parameters on IVD response to axial rotation. The bar charts: difference between the 1 and the 4 cases (the 2 and 3 for the hatched area) normalized to the reference result (ref) obtained with the basic model. The line graph corresponds to the evolution of the apparent stiffness in axial rotation with the different scenarios of 7 parameters.

Table 1: Applied intervertebral range of motion for the relaxation step for each load type. Motion: physiological motion of the whole cervical segment. Intervertebral rotation: C6-C7 rotation with *ILB*:lateral bending, *IFl*: flexion and *IAR*: axial rotation. Intervertebral translation: C6-C7 rotation with *P/A*: posterior(-)/interior(+), *L/R*: left (-)/Right(+) and *D/U*: down (-)/ up (+). For lateral bending and axial rotation, the intervertebral motion values correspond to 10° and 6°, respectively, of the C3-C7 segment and were taken from the curves in the cited reference. For the flexion, the intervertebral motion values correspond to the half of the studied range of motion (59.5° of the C1-T1 segment) in the cited reference.

Motion	Intervertebral rotation (^{o})			Intervertebral translation (mm)			Ref
	ILB (X)	IFl (Y)	IAR(Z)	P/A (X)	L/R (Y)	D/U (Z)	
Lateral bending	1.64	-0.15	-0.18	0.0	-0.34	0.08	[49]
Flexion	1.2	7.5	0.8	0.0	0.0	0.0	[51]
Axial rotation	1.1	-0.8	-0.3	0.1	-0.3	0.1	[49]

Table 2: Model parameters values for the basic model and the cases used for the parametric study. Variation of each parameter of this list was separately tested.

	Parameter	Basic	Cases				References used in the definition
			1	2	3	4	of the intervals of study
NP	μ_{NP} (MPa)	0.4	0.1	0.25	0.55	0.7	[58, 53]
	λ_{NP} (MPa)	0.3	0.1	0.2	0.4	0.5	[58, 53]
	$k0_{NP}^{\times 10^{-4}}$ $(mm^4/(Ns))$	13	3	8	18	23	[52, 57]
	C_{fc0} (mol/m^3)	300	-				[58]
	ϕ_0	0.8	-				[58]
AF ground substance	μ_{AF} (MPa)	1.2	0.4	0.8	1.6	2	[7, 57]
	λ_{AF} (MPa)	1.3	0.2	0.75	1.85	2.4	[70, 4]
	$k0_{AF}^{\times 10^{-4}}$ $(mm^4/(Ns))$	13	3	8	18	23	[52, 57]
	C_{fc0} (mol/m^3)	150	-				[11]
	ϕ_0	0.7	-				[58]
AF fibrillar network	a_{AF} (MPa)	1.2	0.3	0.75	1.65	2.1	[52, 54]
	b_{AF}	350	50	200	500	650	[11, 8]
	$\Delta\alpha$	5	0	2.5	7.5	10	[52, 71]
	K_{AF}	0.166	-				
CEP	μ_{CEP} (MPa)	7.14	-				[70]
	λ_{CEP} (MPa)	10.44	-				[70]
	$k0_{CEP}^{\times 10^{-3}}$ $(mm^4/(Ns))$	3.5	-				[70]
	C_{fc0} (mol/m^3)	90	-				[11]
	ϕ_0	0.8	-				